IOP Publishing Phys. Med. Biol. 65 (2020) 045013 (11pp) https://doi.org/10.1088/1361-6560/ab63ef

Physics in Medicine & Biology

IPEM Institute of Physics and Engineering in Medicine

PAPER

RECEIVED
21 October 2019

REVISED
14 December 2019

ACCEPTED FOR PUBLICATION
19 December 2019

PUBLISHED
13 February 2020

Novel preclinical PET geometrical concept using a monolithic scintillator crystal offering concurrent enhancement in spatial resolution and detection sensitivity: a simulation study

Amirhossein Sanaat[1], Hossein Arabi[1], Mohammad Reza Ay[2,3] and Habib Zaidi[1,4,5,6,7]

[1] Division of Nuclear Medicine and Molecular Imaging, Geneva University Hospital, Geneva CH-1211, Switzerland
[2] Department of Medical Physics and Biomedical Engineering, Tehran University of Medical Sciences, Tehran, Iran
[3] Research Center for Molecular and Cellular Imaging, Tehran University of Medical Sciences, Tehran, Iran
[4] Geneva University Neurocenter, Geneva University, 1205 Geneva, Switzerland
[5] Department of Nuclear Medicine and Molecular Imaging, University of Groningen, University Medical Center Groningen, Groningen, The Netherlands
[6] Department of Nuclear Medicine, University of Southern Denmark, DK-500, Odense, Denmark
[7] Author to whom any correspondence should be addressed.

E-mail: habib.zaidi@hcuge.ch

Keywords: preclinical PET, Monte Carlo simulation, monolithic crystal, spatial resolution, sensitivity

Abstract

We propose a small-animal PET scanner design combining two sets of monolithic crystals with two different thicknesses. The detectors with thinner crystals serve for high resolution imaging while the thicker crystals retain the detection efficiency. Two small-animal PET models based on 10 and 12 detector blocks made of monolithic LYSO crystals were implemented in the GEANT4 Monte Carlo toolkit. In each of these models, half of the detector blocks consisted of a crystal thickness of 10 mm whereas the second half had a crystal thickness of 2 mm. The scintillator crystals were coupled to SiPM arrays. For the first model, the detector blocks were arranged in a full-ring polygonal geometry in such a way that detector blocks with the same thickness were sitting opposite to each other. For the second model, detector blocks with different crystal thicknesses were facing each other. The performance of the proposed PET models was assessed using standard parameters, including spatial resolution, sensitivity and noise equivalent count rate. Comparison was made with conventional PET models with crystal thicknesses of 2 mm, 6 mm and 10 mm. PET models with a crystal thickness of 2 mm led to the highest spatial resolution (up to 0.6 mm FWHM) at the cost of poor absolute sensitivity (2.5%). On the other hand, PET models with a crystal thickness of 10 mm led to good detection efficiency (4.4%), yet with substantial degradation of spatial resolution (1.2 mm FWHM). The proposed PET models with thick and thin crystals exhibited an optimal trade-off between spatial resolution and sensitivity outperforming the PET model with fixed 6 mm crystal by achieving a spatial resolution of 0.7 mm and absolute sensitivity of 3.7%. The novel proposed PET design concept achieved an optimal trade-off between the sensitivity and spatial resolution by combining two sets of monolithic crystals.

1. Introduction

Over the last two decades, biomedical research using animal models of human disease has witnessed a fast growing pace. Animal dissection used to be the common practice to examine disease progression, feedback and response to treatment at several time points, which required large cohorts of animals to enhance the statistical confidence in findings/outcomes. High resolution dedicated PET scanners designed for small animal imaging enabled longitudinal examination on relatively small numbers of animal with sufficient quantitative and statistical accuracy. The potential of radiotracer-based molecular imaging offered by PET has rendered this modality a powerful and indispensable tool in preclinical research (Zaidi 2014).

There is an increasing demand for higher spatial resolution and sensitivity in small animal PET scanners to properly track and quantify physiologic processes (Levin and Zaidi 2007). To achieve a high spatial resolution, detector modules composed of discrete small detector components are commonly utilized to increase the number of samples taken in the spatial domain (Cutler *et al* 1992, Stortz *et al* 2017). However, joints or gaps (dead areas) existing between the detector components and/or modules reduce the sensitivity and, in some cases, produce artifacts (Nagarkar *et al* 2004, Kuang *et al* 2018). Moreover, manufacturing detector modules with very small scintillator elements to enhance the spatial resolution would considerably add to the cost of the PET scanner. Despite the complex production procedure, the detector elements' size in pixelated PET detectors has been reduced down to 0.5 mm compared to early designs using 1–2 mm (Stickel *et al* 2007, Marcinkowski *et al* 2016). However, these detectors suffer from mediocre sensitivity owing to the increased ratio of dead area (joints between the detector elements) to the total sensitive area.

One way to overcome the drawbacks associated with pixelated PET detector arrays is to employ monolithic scintillator crystals, which are capable of providing relatively high detection efficiency. In monolithic scintillators, the improved detection sensitivity is achieved by the uniform detection medium without dead joints between adjacent detector components (Schaart *et al* 2009, Espana *et al* 2014). In addition to lower production cost and easier accessibility to the end-users, monolithic scintillator detectors potentially offer the unique capability of depth-of-interaction (DOI) estimation, thereby improving the spatial resolution. The shape of the light photon distribution over the photodetectors attached to the monolithic scintillator is correlated with the position of photoelectric events, which can be utilized to estimate the DOI (González-Montoro *et al* 2017). These properties of monolithic crystals have made them an attractive option for use on commercial animal PET scanners (Lewellen 2008).

There is predominantly a trade-off between spatial resolution and detection sensitivity imposed by the thickness of the detector elements. Thicker detector elements provide improved detection sensitivity as it is less likely that photons pass through the crystals without interaction. This issue plays a more important role when photons with higher energy, and consequently lower linear attenuation coefficient, are supposed to be detected. However, increasing the thickness of the detector elements would influence the accuracy of the estimated position of interaction owing to increased parallax effect (Xu *et al* 2019).

Substantial efforts focused on the improvement of detection efficiency of the PET detector modules aiming at enhancing image quality and/or diminishing the injected activity. Geometrically speaking, increasing the axial field-of-view (FOV) of the scanner and hence the solid angle coverage, would enhance the detection efficiency with minor or no degradation of the spatial resolution. An extreme form of this design concept was implemented in the total-body EXPLORER PET scanner with an axial coverage of ~2 m (Cherry *et al* 2018). This scanner achieved increased detection sensitivity up to 40 times compared to conventional PET scanners (Zhang *et al* 2017). Moreover, non-conventional geometry PET scanners have been proposed to either enhance the detection efficiency of the scanner or reduce the number of detector elements (for the sake of higher cost efficiency) or both. For instance, the D-shape PET scanner design provided 30% increase in detection sensitivity as well as 12% decrease in the number of required detector elements relative to regular ring shape scanners (Ahmed *et al* 2017). Likewise, for dedicated brain PET scanners, there is a tendency towards geometries offering optimal coverage of the head with minimal dead (unused) FOV, such as the ECAT HRRT brain scanner (Eriksson *et al* 2002). This scanner has a gantry of 35 cm in diameter, which provides axial and transaxial FOVs of 25 and 31 cm, respectively, to cover the entire head. More specifically, the helmet PET scanner, equipped with multiple detector arrays to closely surround the entire head region, has been introduced to offer a unique increase in detection efficiency by adapting the FOV to the shape of the head. This scanner enabled detection sensitivity boost by up to four-fold compared with conventional PET scanners (Tashima and Yamaya 2016).

Most dedicated small-animal PET scanners were designed and manufactured based on pixelated detector arrays to provide high spatial resolution. Owing to the availability of pixelated detector arrays with small detector elements, sub-millimetric spatial resolution has been achieved (Fontaine *et al* 2009, Prasad *et al* 2011, Sajedi *et al* 2018). However, despite the enhanced spatial resolution, PET scanners equipped with pixelated detector arrays suffer from mediocre or poor sensitivity owing to low detection efficiency of pixelated detector arrays. The typical sensitivity of these scanner varies from 0.61% to 2.8% (Goertzen *et al* 2012), going up to 7.4% (Constantinescu and Mukherjee 2009) and 9.3% (Gu *et al* 2013) for more recent PET scanners with pixelated crystal-based designs.

As opposed to pixelated detector arrays, monolithic scintillators allow achieving high sensitivity at the cost of spatial resolution loss. Few small-animal PET scanners designed based on monolithic crystals achieved competitive performance with respect to pixelated designs (Miyaoka *et al* 2011, Carles *et al* 2012, Sanaat *et al* 2019). For instance, the DigiPET scanner equipped with 2 mm thickness scintillator crystal achieved a spatial resolution of 0.5 mm (Espana *et al* 2014). To the best of our knowledge, there is no brain PET scanner based on monolithic scintillator. The only whole-body PET scanner equipped with a continuous crystal is the J-PET with an axial coverage of 1 m, a spatial resolution of about 3 mm and a sensitivity of 14.9 cps kBq^{-1} at the center of the

FOV (Moskal *et al* 2014). The β_CUBE is a compact preclinical PET scanner for total-body imaging equipped with 8 mm thick monolithic LYSO scintillators that showed a spatial resolution and absolute peak sensitivity of 0.76 mm and 10.2% at the centre of the FOV, respectively (Krishnamoorthy *et al* 2018). Despite the appealing detection sensitivity, limited spatial resolution achieved by monolithic scintillators has restricted their use in the preclinical and clinical PET instrumentation domain. Despite imperfect spatial resolution, monolithic scintillators are an attractive option owing to their high sensitivity and cost effectiveness.

In this work, we investigated the key performance parameters of a number of small-animal PET models designed based on monolithic scintillator crystals. The major distinction between the different models is in the thickness of the monolithic crystal as well as their arrangement within the PET gantry. The main objective is to introduce a novel PET model based on monolithic crystals enabling to establish an effective resolution-sensitivity trade-off. These models are designed using 10 and 12 detector blocks of monolithic Lutetium-Yttrium Oxyorthosilicate doped with cerium (LYSO:Ce) crystals. For each of the 10- and 12-detector block PET models, different crystal thicknesses were simulated to study the trade-off between spatial resolution and detection sensitivity. Moreover, novel detector arrangements were proposed in which two sets of detector blocks with different crystal thicknesses were used. Half of the detector blocks have a crystal thickness of 10 mm while the other half have a thickness of 2 mm. The rationale behind the proposal of these configurations is to retain/enhance the spatial resolution (provided by thin detector blocks with 2 mm crystal thickness) and the detection sensitivity (provided by thick detector blocks with 10 mm crystal thickness). To simulate the different PET models, we utilized the physical characteristics and technical specifications of a previously introduced preclinical PET scanner (Sanaat *et al* 2019).

In the first proposed PET model, the detector blocks with different crystal thicknesses were arranged face-to-face in the full-ring polygonal geometry. Contrariwise, in the second model, detector blocks with the same crystal thickness were placed face-to-face (thick in front of thick and thin in front of thin). In addition, two modes of data acquisition were simulated: stationary and rotating. The gantry had no motion in the stationary mode; however, in the rotating mode, the gantry recurrently rotates with angular steps of 18° and 15° in the first and second configurations, respectively, during the scanning time. These models were simulated using the GEANT4 Monte Carlo (MC) toolkit (Agostinelli *et al* 2003) to measure the spatial resolution and sensitivity based on the NEMA NU4-2008 protocols (National Electrical Manufacturers Association, 2008).

2. Materials and methods

2.1. Geometrical PET configurations

The main objective of this work is to propose novel configurations or arrangements of detector blocks in preclinical PET scanners aiming at achieving better trade-off between spatial resolution and sensitivity scanning. The motivation behind the proposed design concept lies in the use of two monolithic scintillators with different thicknesses (thin and thick) to build the proposed PET scanner. Thick scintillators, having relatively higher detection efficiency, are utilized to maintain/boost the sensitivity, whereas thin scintillators are exploited to retain/enhance the spatial resolution of the scanner. In this regard, two principal configurations can be conceived depending how the thin and thick detectors are arranged: (i) the detector blocks with the same crystal thickness are set face-to-face, and (ii) the detector blocks are arranged such that the detectors with different thicknesses face each other. These two configurations were modeled using 10 and 12 detector blocks (figure 1). The primary incentive behind the choice of 10 and 12 detector blocks in these two configurations is to maintain the symmetry of acquisition. For instance, in the second configuration (figure 1(c)), if the ten detector blocks are used (instead of twelve), the geometry of the scanner will not be symmetric. Moreover, in addition to these two stationary configurations, the rotating configuration is proposed which involves rotation of the gantry by angular steps of 18° in the middle of the scan course. This configuration is intended to homogenize the spatial sampling of the object under study through equal division of the acquisition between thin and thick detector blocks. The rotating configuration is proposed to render the spatial resolution uniform in the image domain through equally sampling by the thin (high resolution) and thick (low resolution) detector blocks.

2.1.1. PET model with 10 detector blocks

In this model, referred to as 10B-10-2, five detector blocks containing thick (10 mm) scintillator crystals were set opposite to five detector blocks with thin crystals (2 mm) as illustrated in figures 1(a) and (b). As mention earlier, in this model, each pair of annihilation photons is most likely detected by opposing thin and thick crystals. Thereby the detection sensitivity and spatial resolution are maintained at the highest achievable level. The same detector blocks but with different thicknesses were used in this model, which consisted of monolithic LYSO crystals with $50.2 \times 50.2\,mm^2$ entrance area, coupled to a Silicon photomultiplier SiPM (Sensl ArrayC-30035-144P-PCB) with 12×12 array size and 4.2 mm pixel pitch. A barium sulfate ($BaSO_4$) reflector material with a thickness of 0.1 mm was used to warp the crystal (figures 1(e) and (f)).

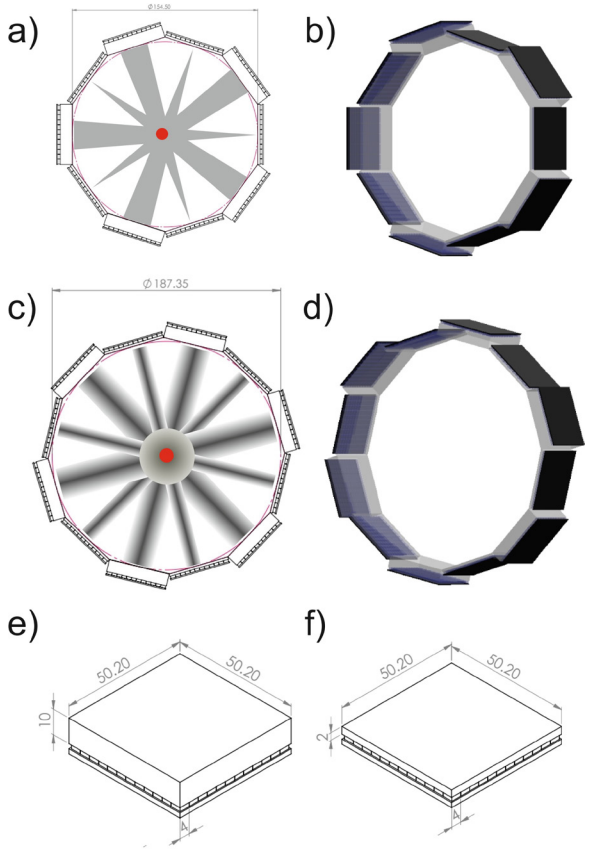

Figure 1. Schematic sketch and 3D view of the PET models with thin and thick detector blocks. (a) PET model with 10 thin (2 mm) and thick (10 mm) detector blocks (10B-10-2) and (b) the corresponding 3D visualization. (c) PET model with 12 thin (2 mm) and thick (10 mm) detector blocks (12B-10-2) and (d) the corresponding 3D visualization. e) The detector block (thick) with crystal thickness of 10 mm and (f) the detector block with crystal thickness of 2 mm.

The performance of this design concept was evaluated against three conventional PET configurations with fixed scintillator thickness. To this end, three detector blocks with thicknesses of 2 mm, 6 mm and 10 mm were simulated using the same geometrical configuration. The PET model with 10 detector blocks and 2 mm crystal thickness, referred to as 10B-2, would offer high spatial resolution owing to the thin detection medium. On the other hand, the PET model with crystal thickness of 10 mm (10B-10) is expected to have the highest sensitivity at the cost of degraded spatial resolution. The PET model with a crystal thickness of 6 mm (10B-6) is expected to exhibit an intermediate performance compared to 10B-10 and 10B-2 models in terms of resolution/sensitivity trade-off. In addition to these models, the rotating version of 10B-10-2 was implemented (10B-10-2-R) where the gantry undergoes a rotation of 18° in the middle of acquisition to render the spatial sampling uniform across the whole FOV. For instance, when thick crystals are facing each other, despite the increased sensitivity for certain lines of response (LORs), the resolution would be deteriorated owing to the sampling with thick crystals. To tackle this issue, the 10B-10-2-R model was proposed to evenly distribute the spatial sampling between the thin and thick detector blocks.

2.1.2. PET model with 12 detector blocks

The PET model consisting of 12 detector blocks differs from the 10B-10-2 model in the sense that the crystals with the same thickness are set in front of each other (thick-to-thick and thin-to-thin) as illustrated in figures 1(c) and (d). The motivation behind the proposal of the PET model with 12 detector blocks (12B-10-2) is that this configuration cannot be implemented using 10 detector modules as the scanner will not be symmetrical since the two modules with the same crystal thickness will be placed next to each other. Disregarding the number of detector blocks, the physical and technical characteristics of the detectors in 12B-10-2 are similar to those of the 10B-10-2 model (table 1). Only the gantry diameters are different due to the different number of detector blocks used.

Similar to the previous section, to assess the performance of the 12B-10-2 model, the 12-detector block models with a crystal thickness of 2 mm (12B-2), 10 mm (12B-10) and 6 mm (12B-6) were also implemented. The rotating version of this model (12B-10-2R) was also implemented using 15 degrees of rotation. Table 2 summarizes the specifications of the various models implemented using 10 and 12 detector blocks.

Table 1. Physical characteristics of the PET models with 10- and 12-detector blocks.

	10B-models	12B-models
Number of detector blocks	10	12
Crystal type	LYSO—Monolithic	LYSO—Monolithic
Ring diameter	154 mm	187 mm
Axial field-of-view	50.2 mm	50.2 mm
Acceptance angle	36°	30°
SiPM array	12 × 12	12 × 12
SiPM pixel size	3 × 3 mm^2	3 × 3 mm^2
SiPM pixel pitch	4.2 × 4.2 mm^2	4.2 × 4.2 mm^2

Table 2. The number of detectors and crystal thickness for the different PET scanner models.

PET model	Number of detector	Crystal thickness	PET model	Number of detector	Crystal thickness
10B-10	10	10 mm	12B-10	12	10 mm
10B-2	10	2 mm	12B-2	12	2 mm
10B-6	10	6 mm	12B-6	12	6 mm
10B-10-2	5	10 mm	12B-10-2	6	10 mm
	5	2 mm		6	2 mm
10B-10-2-R	5	10 mm	12B-10-2-	6	10 mm
	5	2 mm	R	6	2 mm

2.2. Monte Carlo simulations

Monte Carlo simulations of a PET scanner requires accurate modeling of the transport of scintillation photons traveling towards the photodiodes, the physical interaction of annihilation photons occurring within the crystal, the scintillation process and the effect of the readout electronics which convert the light signal into electrical signal. To this end, the Monte Carlo simulations of the above-mentioned PET models was performed using the GEANT4 (version 4.10.2) code (Agostinelli *et al* 2003). Moreover, optical transport was also taken into account for a more realistic simulation.

To include optical processes, the following libraries containing the data to track electrons and optical photons were used in the simulation: G4OpRayleigh, G4OpScintillation, G4OpBoundaryProcess, G4OpAbsorption, G4MultipleScattering, G4eIonisation and G4eBremsstrahlung. According to the GEANT4 library protocol, all processes starting with 'G4Op' deal with optical photon interactions whereas those starting with 'G4e' correspond to electron interactions. In addition, the following libraries were added to the simulation to account for photons with ionizing energies: G4LowEnergyCompton, G4LowEnergyRayleigh and G4LowEnergyPhotoElectric (Allison *et al* 2006, 2016). The reflection of scintillation photons at the boundaries between the two dielectric materials were accurately modeled using the UNIFIED model in GEANT4 (Nayar *et al* 1991).

It was assumed, in this simulation, that all photons are reflected with a reflectivity of 97% on the surface of the reflector based on the employed 'Paint' model (van der Laan *et al* 2010). Similarly, the 'Ground' model (Levin and Moisan 1996, van der Laan *et al* 2010) was utilized for surfaces interfacing the LYSO crystal and glue as well as glue and SiPMs. Refractive indices of 1.82, 1.42 and 1.6 were used for LYSO crystals, glue and SiPM, respectively. It is worth mentioning that in the Ground model surface of GEANT4, if an optical photon reaches the boundary of two materials composed of different compounds, it is either refracted or reflected with a certain probability calculated based on refractive indices of the two materials and the incidence angle of the beam. According to the characteristics of the LYSO crystal, provided by the manufacturer, the refractive index of LYSO was set at 1.82 and a light yield of 25 000 optical photons per MeV was considered. The reflectivity and photon detection efficiency of SiPM were set to 20% and 23% (according to the datasheet), respectively. The optical photons reaching the SiPM pixels were considered to create the output signal. For energy discrimination, values of 144 pixels are summed up and only events in the full energy peak are used for positioning calculation.

2.3. Image reconstruction

Data processing was performed using in-house software developed in C++ environment to extract the position of each event in the monolithic crystal based on the Correlated Signal Enhancement (CSE) positioning algorithms. More specifically, we calculated the number of optical photons reaching each of the 144 SiPM pixels. For each scintillation, we summed the number of optical photons reaching the pixels in each row and column separately. Hence, we were able to report the position of each scintillation inside the crystal knowing the two arrays (summation of column—*Y* direction of the SiPM array and row—*X* direction of SiPM array). These two

1D arrays provide the highest probable row and column and their neighbours, which can be used for estimation of the interaction point (Flower 2012, Fard *et al* 2016). The following processes were performed to generate output images. First, true coincidences were recognized based on a time window of 7 ns and an energy window of 400–650 keV. Then, scintillation photons reaching SiPM's pixels were separately stored in a root file for each of the 144 SiPM pixels along with the position information along *X* and *Y* directions. The CSE algorithm was applied to scintillation photons distribution to estimate the origin of scintillation events for each detector block. A line was assumed between two scintillation events as a LOR. The LORs were labeled with their corresponding distance and angulation from the *Z*-axis of the scanner. The single-slice rebinning algorithm was employed to rebin the LORs in the oblique planes to direct plane. The acquired LORs were registered in a sinogram and the reconstruction performed using a 2D filtered back projection (FBP2D) algorithm implemented witin STIR package (Thielemans *et al* 2012).

2.4. Validation and performance evaluation

The PET models implemented in GEANT4 and the image reconstruction code were validated against the empirical data obtained from a prototype small animal PET scanner designed and fabricated in our lab (Amirrashedi *et al* 2019, Sajedi *et al* 2019). The details of the validation procedures are described in our previous study (Sanaat *et al* 2019). Table 3 shows the technical specifications of the prototype PET scanner used for Monte Carlo modeling of the proposed PET models.

The performance of the proposed PET models were evaluated using the NEMA NU4-2008 standard (National Electrical Manufacturers Association 2008). Owing to the long computational time of Monte Carlo simulations, we focused mostly on the assessment of key performance parameters, including the sensitivity, spatial resolution and count rate for the different PET models.

2.5.1. Spatial resolution

The NEMA NU 4-2008 evaluation procedure of the spatial resolution was applied to calculate the point spread function (PSF) of the PET models at different positions. The spatial resolution of the different PET models was estimated using a ^{22}Na point source (4μCi activity and 1 mm diameter). The point source was fixed inside a 1 cm^3 block of acrylic and located at different radial positions along the central axes of the PET ring. The spatial resolution was reported as full width at half-maximum (FWHM) of intensity profiles followed by Gaussian fitting acquired from images of the point source. The point source was located at 5 mm, 10 mm, 15 mm and 25 mm distances from the radial center of the scanner. To examine the impact of parallax error on the spatial resolution across the axial FOV, the spatial resolution measurement was repeated at four points (5 mm, 10 mm, 15 mm and 25 mm) along the radial axes.

2.5.2. Sensitivity

The sensitivity of the PET models was assessed along the axial FOV through multiple scans of a ^{22}Na point source (180 kBq) for an acquisition time of 10 min. The point source was relocated with a step of 5 mm from one end of the axial FOV to the other. The point source activity concentration was selected low enough to ensure that single event counting losses are below 1% and the randoms rate is less than 5% of the true coincidence events rate (National Electrical Manufacturers Association 2008). The simulation was run until at least 10 000 true coincidences per slice were collected.

2.5.3. Noise equivalent count rate (NECR)

According to the NU 4-2008 protocol, the count rate estimation is carried out using a line source filled with F-18 surrounded by high-density polyethylene cylinder. Moreover, the protocol recommends three types of cylindrical phantoms with a height of 60 mm, 160 mm and 390 mm to mimic animal models of mouse, rat and monkey, respectively. In this work, the simulation of the rat and monkey phantoms was not considered since these PET models are intended solely for mice scanning. At each measurement point, the peak of the NECR and the activity at which the peak NECR occurred were recorded using the default energy window of 400–650 keV and a timing window of 4 ns.

3. Results

3.1. Validation

The spatial resolution and sensitivity estimated for the PET models implemented within the GEANT4 simulation platform exhibited good agreement with the experimental measurements performed on the Xtrim small-animal PET scanner. The difference between the simulated and experimental spatial resolution measured at the center of FOV did not exceed 0.1 mm while the sensitivity was estimated with a maximum 0.2% error. The details of the validation procedure are presented in Sanaat *et al* (2019).

Table 3. Physical characteristics and dimensions of the PET scanner used for the validation of the model in GEANT4.

Parameter	Value
Number of block rings	1
Detector blocks per ring	10
Scintillator material	LYSO
Crystals per block	$24 \times 24 = 576$
Axial FOV	50 mm
Transaxial FOV	100 mm
Number of image planes	109
Coincidence time window	4.0 ns
Energy window	150–650 keV
Energy resolution	11.7%
Detector block entrance area	$50 \times 50\,mm^2$
Crystal size (thickness)	$2 \times 2 \times 10\,mm^3$
Detector ring diameter	842 mm
Photodetector	SiPM
Array size	12×12
Pixel pitch	4.2 mm
Reflector material	$BaSO_4$
Thickness	0.1 mm

3.2. Spatial resolution

The spatial resolutions estimated for PET models with 10- and 12-detector blocks are presented in figure 2. The spatial resolution was measured at axial (figures 2(a) and (c)) and radial directions (figures 2(b) and (d)). According to the NEMA NU-4 protocol, the spatial resolution is measured at the center and ¼ axial transverse distance. In this work, additional measurements were performed along the axial and radial directions with a step of 5 mm.

The radial spatial resolutions measured for the 10B-10-2 PET model varied between 0.8 mm and 1.5 mm (FWHM) while the 10B-6 model, considered as the main competitor of the 10B-10-2 model, led to axial spatial resolution variation between 0.9 mm and 1.6 mm FWHM.

In agreement with the results presented in figures 2(a) and (b), the 12B-10-2 model outperformed the 12B-6 model in terms of spatial resolution for all measurement points. Overall, the spatial resolution of the PET models with 12 detector blocks was improved compared to the corresponding models with 10 detector blocks. Moreover, the rotating PET models (10B-10-2-R and 12B-10-2-R) led to significant spatial resolution enhancement compared to the 10B-10-2 and 12B-10-2 models.

3.3. Sensitivity

Figures 3(a) and (b) summarize the absolute sensitivity of the PET models with 10- and 12-detector blocks, respectively. The sensitivity was measured across the axial FOV using the default energy window of 400–650 keV. The highest sensitivity (up to 4.3% and 3.1%) in both configurations was achieved by the 10B-10 and 12B-10 PET models, respectively, owing to the thick scintillator crystals. The 10B-10-2 and 12B-10-2 models led to second highest sensitivity at the center of the FOV. Considering the results obtained from the 10B-6 and 12B-6 models, the 10B-10-2 and 12B-10-2 PET models led to higher sensitivity at most measurement points.

3.4. Noise equivalent count rate (NECR)

The noise equivalent count rate of the different PET models was estimated at the center of the FOV. The mouse-sized phantom, filled with activity varying from 0.1 to 16 MBq, was employed to estimate the true, random, scatter and total count rates. Figures 4(a) and (b) present the NECR estimated for the different PET models with 10- and 12-detector block configurations, respectively. The NECR was found to be around 20 kcps and 16 kcps at an activity of 13 MBq and 11 MBq for 10B-102 and 12B-10-2 configurations, respectively. Moreover, figures 5(a) and (b) illustrate the rate of scatter, true, total, random and NECR for the 10B-10-2 and 12B-10-2 PET models, respectively. The total count rates reached the maximum values of 33 kcps and 25 kcps at around 13.2 MBq activity concentration in both 10B-10-2 and 12B-10-2 PET models.

4. Discussion

The demand for further improvement of key performance parameters of preclinical PET scanners, such as spatial resolution and sensitivity, has been one of the main objectives of active groups in academic and corporate

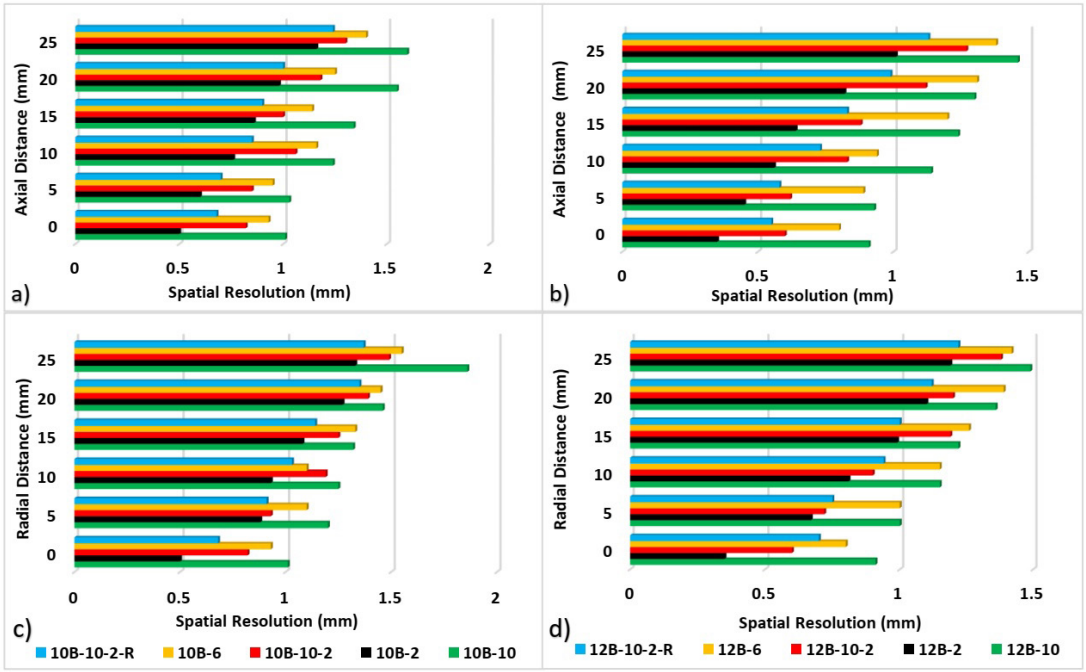

Figure 2. Axial (a) and (b) and radial (c) and (d) spatial resolution estimated for the different PET scanner models.

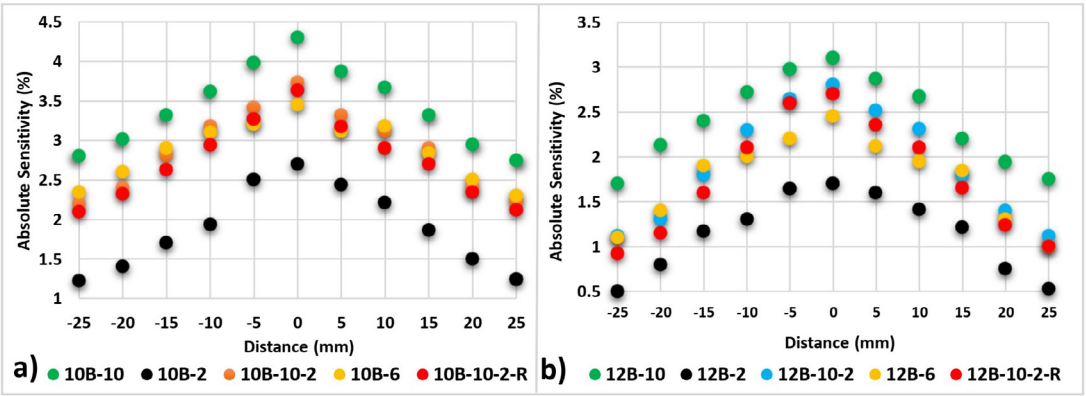

Figure 3. Absolute sensitivity measured at different distances from the center of the FOV along the *Z*-axis for (a) PET models with 10 detector modules and (b) PET models with 12 detector modules.

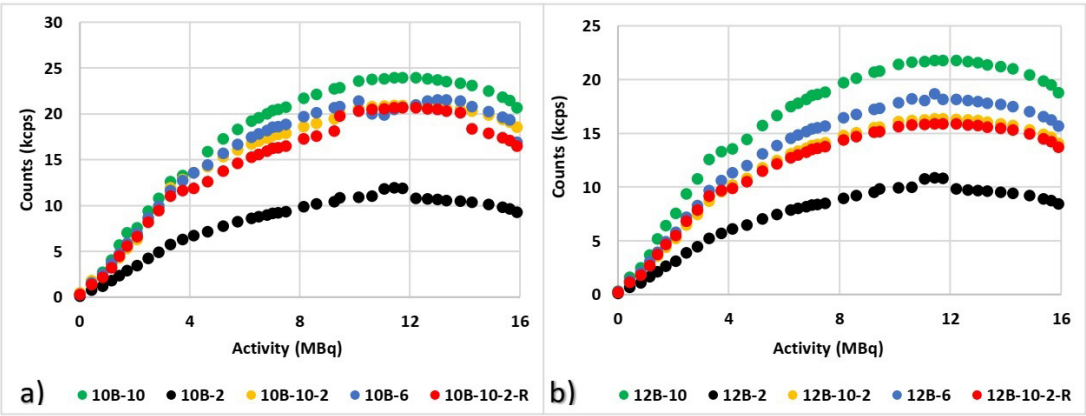

Figure 4. NECR performance for the simulated PET models. (a) Configurations with 10 detector modules and (b) 12 detector modules.

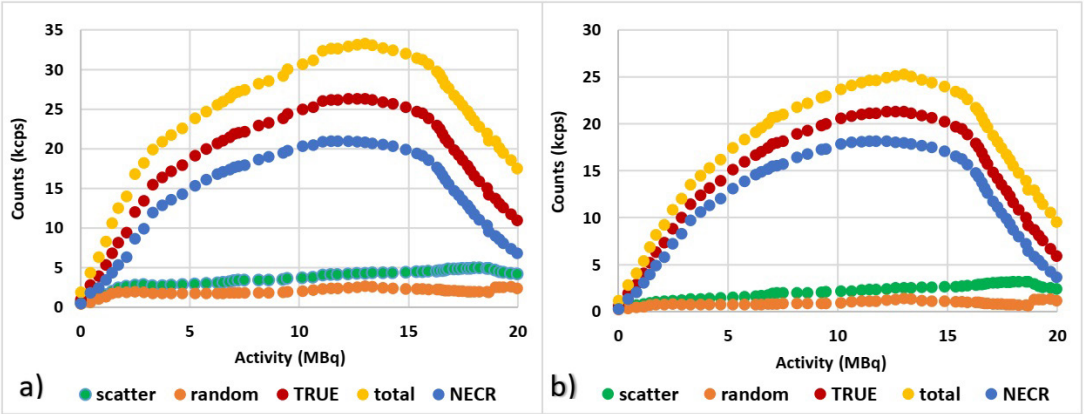

Figure 5. NECR, scatter, random, true, total count rates for (a) 10B-10-2 and (b) 12B-10-2 PET models.

settings. A sub-millimetric spatial resolution is desired for small-animal imaging experiments. Conversely, a high detection sensitivity will lead to shorter scanning time and/or reduced injected activity. In this work, we proposed a novel PET model equipped with two sets of monolithic scintillators with different thicknesses (2 mm and 10 mm). Thick crystals are intended to enhance/maintain the detection efficiency while the thin crystal would compensate the spatial resolution loss caused by thick crystals. This novel PET model aims to achieve an optimal trade-off between detection efficiency and spatial resolution.

It was demonstrated that using only 2 mm thick LYSO crystal (10B-2 and 12B-2 PET models) would result in relatively high axial (0.55 mm, 0.35 mm, respectively) and radial (0.75 mm, 0.6 mm, respectively) spatial resolutions for the above-mentioned PET models at the cost of poor sensitivity (1.6% and 2.6%, respectively). Conversely, using 10 mm crystal thickness would enhance the detection efficiency of the system up to 4.3% and 3.1% for 10B-10 and 12B-10 PET models, respectively. However, the spatial resolution would be limited to 1 mm in the best case. To establish a compromise between the spatial resolution and sensitivity, a PET model with a crystal thickness of 6 mm was investigated. This model achieves a reasonable compromise between the spatial resolution and sensitivity achieved by the 2 mm and 10 mm PET models. However, the proposed PET models (10B-10-2 and 12B-10-2) with thin and thick crystals exhibited a performance beyond this compromise, leading to spatial resolution of 0.9 and 0.6 mm FWHM, respectively, thus outperforming the 10B-6 and 12B-6 PET models with 1.2 to 0.8 mm FHWM, respectively. In addition, a detection sensitivity of 2.8% was achieved with the 12B-10-2 PET model compared to the 12B-6 PET model with a sensitivity of 2.45%. Using a combination of thick and thin crystals reduces the uncertainty on the assigned LOR for one side of paired detectors in configuration #1 and half of the paired detectors with thin crystals in configuration #2. This results in higher positioning accuracy and hence better spatial resolution.

As discussed earlier, the rotating PET models (10B-10-2-R and 12B-10-2-R) were also considered to address the non-uniform spatial resolution across the radial FOV on the 10B-10-2 and 12B-10-2 models owing to the non-symmetrical data acquisition geometry. Image reconstruction algorithms allowing to take into account spatial resolution degradation could enable these proposed PET models to recover a uniform spatial resolution across the FOV (Rahmim *et al* 2013, Zeraatkar *et al* 2014). The non-uniformity of the spatial resolution is expected to be noticeable solely at the boundary of the FOV (particularly for the 10B-10-2 model) since the interplay of the many LORs passing through high and low resolution detectors would render spatial resolution uniform at the center of the FOV. At the boundaries of the FOV, the contribution of a low (or high) resolution LOR might carry greater weight than the others. This phenomenon is expected to disappear in the rotating PET models owing to the uniform distribution of the low and high resolution LORs across the FOV.

The quantitative evaluation demonstrated that the relative differences between the sensitivity of our proposed configurations (10B-10-2 and 12B-10-2) and the conventional configurations (10B-10 and 12B-10) were 1% and 0.5%, respectively. However, the amount of LYSO crystal consumed in the 10B-10 and 12B-10 models decreased from 250 cm^3 and 300 cm^3 to 150 cm^3 and 180 cm^3 in 10B-10 and 12B-10-2 models, respectively. Although the depth of interaction was not taken into account (which warrants further investigation in future work), the spatial resolution achieved by the 10B-10-2 (0.8 mm) and 12B-10-2 (0.6 mm) PET models are comparable with commercially available as well as prototype small-animal PET scanners equipped with pixelated detectors. A 0.5 mm LYSO detector array fabricated for high resolution PET applications led to an intrinsic spatial resolution of 0.68 mm FWHM (Stickel *et al* 2007). The DigiPET scanner based on monolithic LYSO detector (with a crystal thickness of 2 mm), equipped with sub-millimetric DOI precision, achieved a spatial resolution of 0.7 mm FWHM [9]. However, the absolute sensitivity did not exceed 0.3% at center of FOV, which is substantially

smaller than those of the 10B-10-2 model (3.74%) and particularly the 12B-10-2 model (2.8%) (Marcinkowski *et al* 2016).

The count rate performance of the proposed PET models was characterized for a mouse-sized cylindrical phantom following the NEMA standards. For the 10B-10-2 and 12B-10-2 models, the phantom was placed in the FOV such that the line source resided at the center of the two opposing detectors. The 10B-10-2 and 12B-10-2 models achieved a peak NECR of 20 kcps and 16 kcps at 13 MBq and 11 MBq, respectively. Even though the NECR performance of the proposed models lagged behind the 10B-6 and 12B-6 models, this performance parameter, do not play a significant role in mouse PET imaging in practice. The peak NECR for state-of-the-art preclinical PET scanners measured using the mouse phantom is commonly attained within the range 50–200 MBq (Goertzen *et al* 2012). However, these values are 5–20 folds greater than the typical activity commonly used in preclinical setting for mice PET scanning (7.4 MBq). The typical activity injected in mice PET scanning would lead to 75 times higher activity concentration (~370 kBq g^{-1}) compared to human PET imaging (~5 kBq g^{-1}).

The NECR curve presents some spikes and discontinuities instead of being smooth. We also observed that the plot of the sensitivity is slightly asymmetric owing to statistical uncertainties associated with Monte Carlo simulations. MC simulations were ran 10 times for the worst case scenario (configuration two, model 12B_2, point @ +25 mm) resulting in an average sensitivity of 0.51% and standard deviation of 0.086 [range 0.38%–0.63%].

The rotating PET models (10B- and 12B-10-2-R) exhibited similar performance to the 10B- and 12B-10-2 models in terms of spatial resolution and sensitivity. The slight decrease observed in the sensitivity of the rotating PET models is due to rotation time where the detector acquisition is off. Regarding the rotating PET models, an attractive acquisition mode could be realized in these models for high resolution imaging. In this acquisition mode, only 2 mm thick detector blocks are activated while the 10 mm thick detectors remain inactive. Thus, only the high resolution LORs (passing through the thin crystals) are utilized for PET image reconstruction. However, portion of the FOV would not be sufficiently sampled by the high resolution LORs. As such, rotation of the PET detectors is essential in this acquisition mode to complete the sampling of the FOV by the high resolution LORs. This acquisition mode would potentially lead to similar spatial resolution achieved by the PET models with 2 mm crystal thickness (10B-2 and 12B-2) owing to identical LOR definition in these two models. Undoubtedly, the sensitivity of this acquisition mode would be half of the equivalent 10B-2 and 12B-2 PET models since half of the detector blocks are inactive through the acquisition course. Briefly, the rotating models can be operated with two acquisition modes: (i) normal acquisition mode, where all detector blocks are active to achieve an optimal trade-off between spatial resolution and detection sensitivity and (ii) high resolution mode, where only the thin detector blocks are active to enhance the spatial resolution of the scanner (up to those of the PET model with 2 mm crystal thickness) at the cost of halved detection sensitivity.

5. Conclusion

A novel design of small animal PET scanner based on monolithic crystals was proposed to simultaneously enhance the detection sensitivity and spatial resolution. The underlying idea was to use two sets of monolithic LYSO crystals with different thicknesses. The thick crystals (10 mm), intrinsically having higher sensitivity, would retain/enhance the detection efficiency of the scanner. Conversely, the thin crystals (2 mm) enable the scanner to sample the object with high spatial resolution. This novel design achieved an optimal trade-off between the sensitivity and spatial resolution, resulting in a spatial resolution of 0.7 mm and a sensitivity of 3.74% at the center of the FOV.

Acknowledgments

This work was supported by the Swiss National Science Foundation under grant SNRF 320030_176052 and Tehran University of Medical Sciences under grant No. 36291.

ORCID iDs

Amirhossein Sanaat https://orcid.org/0000-0001-8437-2060
Mohammad Reza Ay https://orcid.org/0000-0002-5383-4418
Habib Zaidi https://orcid.org/0000-0001-7559-5297

References

Agostinelli S *et al* 2003 GEANT4- a simulation toolkit *Nucl. Instrum. Methods Phys. Res.* A **506** 250–303
Ahmed A M, Tashima H and Yamaya T 2017 Simulation study of a D-shape PET scanner for improved sensitivity and reduced cost in whole-body imaging *Phys. Med. Biol.* **62** 4107–17

Allison J *et al* 2006 Geant4 developments and applications *IEEE Trans. Nucl. Sci.* **53** 270–8
Allison J *et al* 2016 Recent developments in Geant4 *Nucl. Instrum. Methods Phys. Res.* A **835** 186–225
Amirrashedi M, Sarkar S, Ghafarian P, Shahraki R H, Geramifar P, Zaidi H and Ay M R 2019 NEMA NU-4 2008 performance evaluation of Xtrim-PET: A prototype SiPM-based preclinical scanner *Med. Phys.* **46** 4816–25
Carles M, Lerche C W, Sánchez F, Orero A, Moliner L, Soriano A and Benlloch J M 2012 Performance of a DOI-encoding small animal PET system with monolithic scintillators *Nucl. Instrum. Methods Phys. Res.* A **695** 317–21
Cherry S R, Jones T, Karp J S, Qi J, Moses W W and Badawi R D 2018 Total-body PET: Maximizing sensitivity to create new opportunities for clinical research and patient care *J. Nucl. Med.* **59** 3–12
Constantinescu C C and Mukherjee J 2009 Performance evaluation of an Inveon PET preclinical scanner *Phys. Med. Biol.* **54** 2885–99
Cutler P D, Cherry S R, Hoffman E J, Digby W M and Phelps M E 1992 Design features and performance of a PET system for animal research *J. Nucl. Med.* **33** 595–604
Eriksson L *et al* 2002 The ECAT HRRT: NEMA NEC evaluation of the HRRT system, the new high-resolution research tomograph *IEEE Trans. Nucl. Sci.* **49** 2085–8
Espana S, Marcinkowski R, Keereman V, Vandenberghe S and Van Holen R 2014 DigiPET: sub-millimeter spatial resolution small-animal PET imaging using thin monolithic scintillators *Phys. Med. Biol.* **59** 3405–20
Fard B T, Ay M, Sajedi S, Akbarzadeh A, Kaviani S and Farahani M 2016 Implementation of correlated signal enhancement (CSE) technique for accurate positioning in gamma camera [abstract] *Eur J. Nucl. Med. Mol Imaging* **43** S510
Flower M 2012 *Webb's Physics of Medical Imaging* (Boca Raton, FL: CRC Press)
Fontaine R *et al* 2009 The hardware and signal processing architecture of LabPET™, a small animal APD-based digital PET scanner *IEEE Trans. Nucl. Sci.* **56** 3–9
Goertzen A L *et al* 2012 NEMA NU 4-2008 comparison of preclinical PET imaging systems *J. Nucl. Med.* **53** 1300–9
González-Montoro A *et al* 2017 Performance study of a large monolithic LYSO PET detector with accurate photon DOI using retroreflector layers *IEEE Trans. Radiat. Plasma Med. Sci.* **1** 229–37
Gu Z *et al* 2013 NEMA NU-4 performance evaluation of PETbox4, a high sensitivity dedicated PET preclinical tomograph *Phys. Med. Biol.* **58** 3791–814
Krishnamoorthy S, Blankemeyer E, Mollet P, Surti S, Van Holen R and Karp J S 2018 Performance evaluation of the MOLECUBES β-CUBE—a high spatial resolution and high sensitivity small animal PET scanner utilizing monolithic LYSO scintillation detectors *Phys. Med. Biol.* **63** 155013
Kuang Z *et al* 2018 Development of depth encoding small animal PET detectors using dual-ended readout of pixelated scintillator arrays with SiPMs *Med. Phys.* **45** 613–21
Levin A and Moisan C 1996 A more physical approach to model the surface treatment of scintillation counters and its implementation into DETECT *Conf. Record IEEE Nuclear Science Symp. (2–9 November 1996)* vol **2** pp 702–6
Levin C S and Zaidi H 2007 Current trends in preclinical PET system design *PET Clin.* **2** 125–60
Lewellen T K 2008 Recent developments in PET detector technology *Phys. Med. Biol.* **53** R287–317
Marcinkowski R, Mollet P, Van Holen R and Vandenberghe S 2016 Sub-millimetre DOI detector based on monolithic LYSO and digital SiPM for a dedicated small-animal PET system *Phys. Med. Biol.* **61** 2196–212
Miyaoka R S, Li X, Hunter W, Pierce L A, McDougald W, Kinahan P E and Lewellen T K 2011 Resolution properties of a prototype continuous miniature crystal element (cMiCE) scanner *IEEE Trans. Nucl. Sci.* **58** 2244–9
Moskal P *et al* 2014 Test of a single module of the J-PET scanner based on plastic scintillators *Nucl. Instrum. Methods Phys. Res.* A **764** 317–21
Nagarkar V V, Tipnis S V, Shah K, Shestakova I and Cherry S R 2004 A high efficiency pixelated detector for small animal PET *IEEE Trans. Nucl. Sci.* **51** 801–4
National Electrical Manufacturers Association 2008 *NEMA Standards Publication NU 4—2008. Performance Measurements of Small Animal Positron Emission Tomographs* (Rosslyn, VA: National Electrical Manufacturers Association)
Nayar S K, Ikeuchi K and Kanade T 1991 Surface reflection: physical and geometrical perspectives *IEEE Trans. Pattern Anal. Mach. Intell.* **13** 611–34
Prasad R, Ratib O and Zaidi H 2011 NEMA NU-04-based performance characteristics of the LabPET-8™ small animal PET scanner *Phys. Med. Biol.* **56** 6649–64
Rahmim A, Qi J and Sossi V 2013 Resolution modeling in PET imaging: Theory, practice, benefits, and pitfalls *Med. Phys.* **40** 064301
Sajedi S *et al* 2018 Generic high resolution PET detector block using 12 × 12 SiPM array *Biomed. Phys. Eng. Express* **4** 035014
Sajedi S *et al* 2019 Development and preliminary results of Xtrim-PET, a modular cost-effective preclinical scanner *Nucl. Instrum. Methods Phys. Res.* A **940** 288–95
Sanaat A, Zafarghandi M S and Ay M R 2019 Design and performance evaluation of high resolution small animal PET scanner based on monolithic crystal: a simulation study *J. Instrum.* **14** P01005
Schaart D R, van Dam H T, Seifert S, Vinke R, Dendooven P, Lohner H and Beekman F J 2009 A novel, SiPM-array-based, monolithic scintillator detector for PET *Phys. Med. Biol.* **54** 3501–12
Stickel J R, Qi J and Cherry S R 2007 Fabrication and characterization of a 0.5 mm Lutetium Oxyorthosilicate detector array for high-resolution PET applications *J. Nucl. Med.* **48** 115–21
Stortz G *et al* 2017 Performance of a PET insert for high resolution small animal PET/MR imaging at 7T *J. Nucl. Med.* **59** 536–42
Tashima H and Yamaya T 2016 Proposed helmet PET geometries with add-on detectors for high sensitivity brain imaging *Phys. Med. Biol.* **61** 7205–20
Thielemans K, Tsoumpas C, Mustafovic S, Beisel T, Aguiar P, Dikaios N and Jacobson M W 2012 STIR: software for tomographic image reconstruction release 2 *Phys. Med. Biol.* **57** 867–83
van der Laan D J, Schaart D R, Maas M C, Beekman F J, Bruyndonckx P and van Eijk C W 2010 Optical simulation of monolithic scintillator detectors using GATE/GEANT4 *Phys. Med. Biol.* **55** 1659–75
Xu J *et al* 2019 A preclinical PET detector constructed with a monolithic scintillator ring *Phys. Med. Biol.* **64** 155009
Zaidi H (ed)2014 *Molecular Imaging of Small Animals: Instrumentation and Applications* (New York: Springer)
Zeraatkar N *et al* 2014 Resolution-recovery-embedded image reconstruction for a high-resolution animal SPECT system *Phys. Med.* **30** 774–81
Zhang X, Zhou J, Cherry S R, Badawi R D and Qi J 2017 Quantitative image reconstruction for total-body PET imaging using the 2-meter long EXPLORER scanner *Phys. Med. Biol.* **62** 2465–85